SSC19-XII-05

Optomechanical Design and Analysis for Nanosatellite Laser Communications

Laura Yenchesky, Ondrej Cierny, Peter Grenfell, William Kammerer, Paula Do Vale Periera, Tao Sevigny, Kerri Cahoy
Massachusetts Institute of Technology
77 Massachusetts Ave, Cambridge, MA 02139; (617) 253-7805
laurayenchesky@alum.mit.edu, ondrej@mit.edu, pgrenfel@mit.edu, wi26858@mit.edu, paulavp@mit.edu, sevignyt@mit.edu, kcahoy@mit.edu

ABSTRACT

The CubeSat Laser Infrared CrosslinK (CLICK) mission is a technology demonstration of a 1.5U laser communications terminal for an intersatellite link. The terminal is deployed on a pair of 3U CubeSats in Low Earth Orbit (LEO). The pointing, acquisition, and tracking (PAT) approach includes both coarse and fine systems. The coarse tracking system uses a beacon laser transmitter and receiver camera. The fine tracking system uses a fast steering mirror and quadrant photodiode. The communications transmit and receive paths include a refractive telescope, transmit laser collimator, and avalanche photodetector (APD) receiver. The communications laser full-width, half maximum (FWHM) beam divergence angle is 14.6 arcseconds, and the beacon laser FWHM divergence is 0.75° (2700 arcseconds). The opto-mechanical design process includes prediction & verification of assembly alignment & calibration, thermoelastic effects, structural modes & static loading, and fastener analysis. The opto-mechanical assembly has the sensors and laser transmitters kinematically mounted to enable on-ground calibration to less than 25.4 μm decenter, or 0.1° tip/tilt. The thermoelastic alignment error between the payload and bus star tracker is estimated via finite element analysis to be less than 9 arcseconds. The payload optical bench is designed with custom thermal isolation and control to maintain 20 ± 10 °C. The thermal modeling of the payload is described in detail. Structural static loading and fastener analyses of the CLICK payload under launch loads of 30 G verify margins of safety are greater than 10 and above the recommended values. Modal analyses predict the first resonant frequency to be 888 Hz, above typical vehicle structural vibration ranges with a factor of safety greater than 3.5.

INTRODUCTION

The CubeSat Laser Infrared CrosslinK (CLICK) mission will demonstrate full-duplex laser communications crosslink between two nanosatellites in Low Earth Orbit (LEO). The mission is a collaboration between the MIT Space, Telecommunications, Astronomy, and Radiation (STAR) Lab, the University of Florida Precision Space Systems Lab (PSSL), and NASA Ames Research Center (ARC). CLICK plans two separate flights of three 3U CubeSats: CLICK-A (one 3U) and CLICK-B/C (two 3Us). CLICK-A will demonstrate an optical downlink at >10 Mbps from a 3U CubeSat to a portable 30 cm ground telescope from LEO as a risk-reduction demonstration of components in the transmitter. CLICK-B/C is a pair 3U CubeSats, each hosting one 1.5U laser communications payload. CLICK-B/C will demonstrate the optical crosslink, which is the focus of this work.

The CLICK technology demonstration will enable future coordinated nanosatellite missions. For example, one application may involve onboard image processing that combines images from multiple spacecraft, which is useful for disaster monitoring, severe weather sensing, and surveillance, as well as commercial applications. The baseline mission crosslinks use laser communications (lasercom) at ranges from 25 km to 580 km with a full-duplex optical link at >20 Mbps. CLICK-B/C CubeSats are designed to support ranging precision of less than 50 cm in addition to precision pointing, acquisition, and tracking.[1] Thermally, the system will remain operational within the range of -10 °C to 40 °C during all mission phases. The payload is estimated to consume a peak power draw during full-duplex lasercom operations of less than 30 W.

Existing Optomechanical Design in CubeSats

Several CubeSat payload optomechanical designs can be found in the literature. These include the Arcsecond Space Telescope Enabling Research in Astrophysics (ASTERIA) whose payload uses precision translational mounting orthogonal to the optical axis.[2] The Snow and Water Imaging Spectrometer (SWIS), a 4U CubeSat payload, capitalizes on kinematic connections to avoid distortion in the optomechanical structure.[3] The SWIS payload structure is constructed out of 6061-T6 Aluminum with isolation to passively control the thermal environment. The PRecursore IperSpettrale della Missione Applicativa (PRISMA) payload design addresses thermal exchange between the spacecraft and payload housing a hyperspectral instrument.[4] The German nanosatellite Experimental Spacecraft based on Nanosatellite Technology (ERNST) manages the thermal gradient between opposite spacecraft panels.[5] The NASA Optical Communications and Sensors Demonstration (OCSD) estimates pointing error from a multitude of sources.[6] Fuchs explains the hybrid approach of the OSIRIS4 Cubesat, which has a planned pointing accuracy within $\pm 1^{\circ}$.[7]

The CLICK-A payload leverages the Nanosatellite Optical Downlink Experiment (NODE) design. NODE is the precursor project from which the CLICK mission evolved. The CLICK-B/C optomechanical design takes inspiration from another MIT CubeSat, the Deformable Mirror Demonstration Mission (DeMi) mission.[8] The CLICK-B/C payload also uses similar compact mechanical housings as were designed for the NODE project.[9] The initial work on the CLICK-B/C payload optomechanical design is captured in the master's thesis by *Long*,[10] which details the initial optomechanical & PAT systems design, the optical configuration & ray-tracing analysis, as well as thermal & thermoelastic analysis. This paper builds on the work in *Long* in the areas of optical layout configuration, kinematic mount design, and thermal & thermoelastic analysis. This paper also details results in structural modes, static loading, and fastener analysis.

Overview of CLICK Optomechanical Design

CLICK mission requirements drive the optical subsystem design and requirements developed in *Long*. The requirements in *Long* are also used in this work.[10] The payload, including optical and electrical components, is limited to 1.5U in volume and 2.5 kg mass, as shown in Fig. 1. The optomechanical design of the CLICK payload meets these strict Size, Weight, and Power (SWaP) requirements to enable the technology to be implemented on a CubeSat.

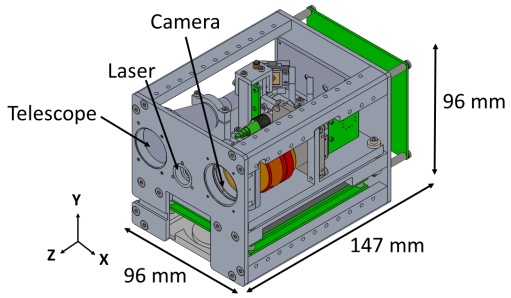

Figure 1: Isometric view of CLICK payload.

The optical subsystem necessary for the CLICK mission has precise alignment requirements. Tolerance position values must accommodate decentering and piston allowances of some components of 25.4 μm and angular alignment must accommodate down to 0.1° of allowable rotation from the ideal positions.[10] Some optical position requirements are satisfied by machine tolerances; however, other components require adjustable mounting techniques to achieve the required precision.

Kinematic mounting constrains all degrees-of-freedom (DOF) of a rigid body without overconstraint.[11] In the kinematic mounts on the CLICK payload, two of the points of contact are adjustable through the use of hex adjusters, and the remaining points of contact are fixed with a ball bearing or constrained with fasteners, as seen in Fig. 2. The kinematic mounting system for CLICK optical components has a translational resolution down to ± 15 μm. However, the decision to use kinematic mounts requires a trade between the volume and precision. Kinematic mounting will be discussed extensively later in this work. The design of the CLICK payload, seen in Fig. 1, aims to leverage precision optomechanical design principles and techniques, including kinematic mounting, to produce two flight units that satisfy mission requirements.

APPROACH

Pointing Budget Influence on Design and Simulations

The crosslinks CLICK-B/C plans to perform will use a full-width-half maximum (FWHM) 14.6 arcsecond communications laser and a FWHM 0.75 degree beacon laser.[1] Pointing error is budgeted in a statistical model to track the power loss due to pointing and verify that it is within link requirements. There are two classes of pointing error, (i) static or very

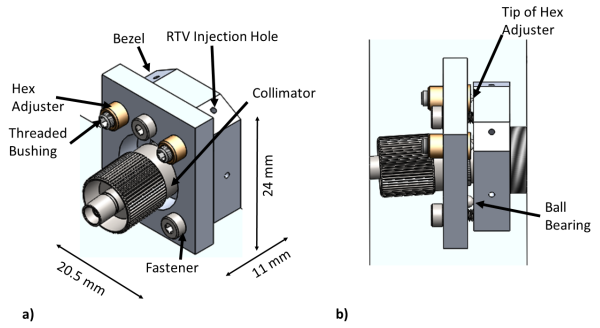

Figure 2: a) Isometric view and b) angled view of computer-aided design (CAD) model of a collimator with a kinematic mount. The kinematic mount allows rotation via tip/tilt of the optical component. The remaining four DOF are not needed for this optical component, and are not adjustable with this mount.

low frequency bias errors and (ii) dynamic, high-frequency jitter errors. Opto-mechanical misalignments due to assembly, launch shift, and thermoelastic effects fall into the static category. Aspects of mechanical design and analysis for the static category of errors are presented in this work. Additional information on pointing budgets for the CLICK mission can be found in *Long*[10] and *Grenfell et al.*[1] General background on pointing budget development can be found in *Hemmati et al.*[12]

The beacon pointing budget in the course pointing system (CPS) has an optomechanical allocation of 495 arcsec (3σ).[10] This requires a sub-allocation for the thermoelastic deformation of the spacecraft bus structure, which is 295 arcseconds from a first order analysis described in the following. This thermoelastic shift changes the relative alignment between the payload and star tracker on the bus, creating pointing error that must be tracked in the pointing budget. *Long* approximates the maximum relative angular displacement in a single axis as a result of the thermal gradients across the bus, modeled as a cantilever beam, with Eq. (1):[10]

$$\theta = \frac{\alpha \Delta T \cdot L}{d} \tag{1}$$

where:

$\alpha \equiv$ the CTE of the Aluminum structure

Ł $\equiv$ length of the satellite

$d \equiv$ width of the satellite

$\Delta T \equiv T_1 - T_2$, change in temperature across spacecraft

This first order hand calculation estimates the maximum misalignment induced by thermoelastic effects as 234 arcseconds. Given this expected value of 234 arcseconds, *Long* allocates 295 arcseconds to thermoelastically induced pointing error in the coarse pointing budget.[10]

Table 1: Optical Components

Abbreviation	Optical Component Name	Kinematic Mount Req.?
L1	Telescope Primary	No
L2	Telescope Secondary	No
FSM	Fast Steering Mirror	No
D1	1st Dichroic (Quadcell)	No
Filt	Filter	No
Quad	Quadcell	Yes
D2	2nd Dichroic (Tx. Laser)	No
Tx. Laser	Transmitting Collimator	Yes
La	APD Focusing Lens	No
APD	Avalanche Photodiode	Yes
Bcn. Laser	Beacon Collimator	Yes
Camera	Camera	No

Verification of the thermoelastically induced misalignment between the payload optics and the spacecraft reference frame is necessary. To accomplish this, thermoelastic modeling of a representative spacecraft bus is conducted using Thermal Desktop®, Femap®, and MATLAB®. These analyses will continue to be iterated upon as the spacecraft structure and thermal parameters are further defined in collaboration with the bus vendor. Thermoelastic modeling and analysis of the spacecraft provides estimates of thermally induced misalignment between the spacecraft frame and payload frame; physically, this is between the star tracker apertures and the payload apertures.

The optical instrument requires sound structural and fastener design. Optical component alignment tolerances as tight as 25.4 μm of decentering and piston translation and less than 0.1° of allowable rotation from the ideal positions are required.[10] Kinematic mounts placed at the most sensitive locations in the system enable precision calibration of the payload on the ground. It is critical that the kinematic mounts, along with all other payload components, will not deform sufficiently to cause a beacon pointing loss due to static and dynamic loading.

The launch environment is considered with respect to static, dynamic, and thermal loading. Only static and dynamic loading are considered in this work. Launch vehicles characterize the expected maximum axial accelerations for a payload as well as the structural-borne random vibrations experienced by a payload. The launch vehicle for CLICK is not known at the time of this writing. The payload is designed to meet NASA General Environmental Verification Standard (GEVS) environments. The Minotaur IV family of vehicles is shown as a specific example launch vehicle case. The maximum axial acceleration as a function of payload mass on a Minotaur IV family vehicle is shown in Fig. 3, as released by Orbital ATK.[13] The maximum steady state axial acceleration for a payload during launch on a Minotaur IV vehicle is approximately 11 G's.[13] Another vehicle example is the Ariane 5 launch system, which specifies maximum longitudinal acceleration at 4.55 G's.[14]

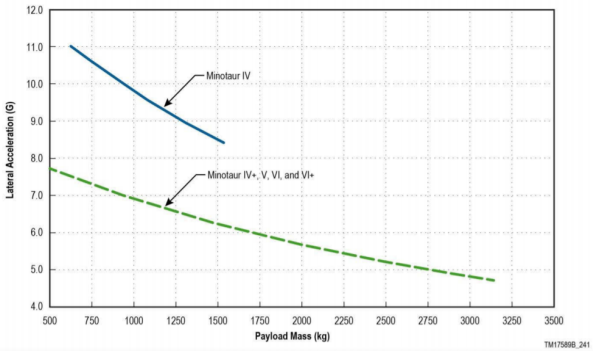

Figure 3: Minotaur IV family maximum axial acceleration as a function of payload mass

The launch load used as an input into the structural and fastener design for CLICK-B/C is 30 G's for a conservative margin. Simulating the effect of these loads on the payload and ensuring that all margin of safety (MOS) are greater than 0 ensures that the payload will not plastically deform on launch and that all fasteners will not separate, yield under shear stress, or yield under tensile stress.

The random structural vibration environment is dependent on the launch vehicle. The Ariane 5 and Minotaur IV user guides specify random structural vibration as occurring below 100 Hz and 250 Hz, respectively.[13,14] A modal analysis is conducted to verify that all resonant frequencies of the CLICK payload are expected to be greater than 250 Hz with margin.

Design Profile

Several payload layout options are considered in order to accommodate the 1.5U payload volume limit. The selected layout has a volume of 96 mm x 96 mm x 147 mm and has an estimated mass of 1.5 kg. The layout is shown in Fig. 4. The optical telescope and camera point out of the +Z (96 mm x 96 mm) face, with board stacks underneath (on the –Y face) and behind the optical bench (on the -Z face). The area allocated to the optical bench coupled with the optical design specifications allocates many of the optical components into a small volume, approximately 95 mm x 56 mm x 119 mm, as seen in Fig. 4. Iterations of optical component mounts are motivated by assembly concerns. For example, the bend radii in the fiber routing must be greater than 15 mm and hex adjusters in the kinematic mounts must be accessible.

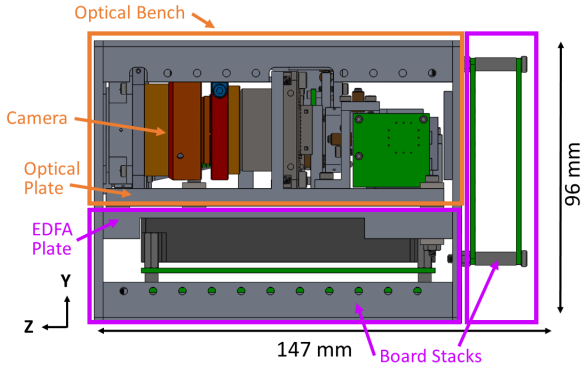

Figure 4: Side View of +X of CLICK Payload

A CAD model for the payload was developed using Solidworks®. The payload mechanical design has been iteratively developed to satisfy interface requirements and evolutionary changes to the payload. Simulation tools are being used to validate aspects of CLICK's design. Thermoelastic modeling and analysis of the spacecraft provides estimates of thermally induced misalignments between the spacecraft and payload optical components. Modal and static loading analyses are conducted on finite element models. Hand calculations for separation and shear fastener analysis estimate the margins of safety.

One engineering model of the entire payload will be fabricated using flight representative materials, assembled, and tested to prototype qualification levels in accordance with NASA GEVS.[15] All structural components shall demonstrate positive margins of safety when exposed to the prototype qualification levels. After the engineering model is assessed, two flight models of the payload will be fabricated, tested

to acceptance levels, and delivered.

SIMULATION SETUP AND ANALYSES

Simulation of the CLICK structural design is used to verify subsystem requirements and predict performance in the launch and space environments. Tight mounting tolerances motivate implementation of precision mounting techniques. The effect of thermoelastically induced shift between the payload and star trackers is analyzed to verify allocations in the coarse pointing budget. The launch environment motivates the structural analysis.

Optical Component Mounting and Layouts

The CAD model includes optical, structural, and electrical components. The 12 optical components are shown in Fig. 5.

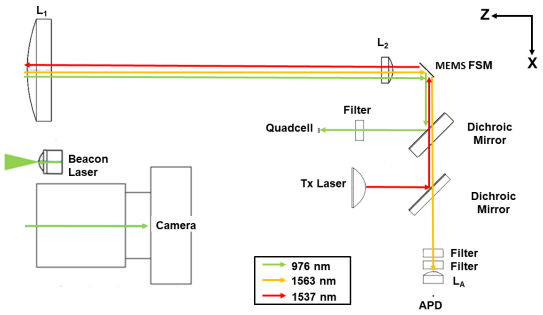

Figure 5: Optical components with spacing and optical path. The leftmost point of L_1 to the center of the MEMS FSM spans 99.71 mm in the Z direction. The center of the MEMS FSM to the avalanche photodiode (APD) focal point spans 53.66 mm.

The components each require mounting individually that meets the positional and rotational tolerance requirements. The system of optical components must be aligned in a method that produces a viable optical path, a feasible mechanical layout of the components and their mounts, and maintains alignment through structural and thermal loading conditions. Fig. 6 shows the assembly of the optical components on the optical bench. Table 1 lists all of the optical components on the optical bench.

Mounting Optical Components

Of the 12 optical components, some are procured unmounted. Custom optical mounts for these components are designed to include a bezel, mounts that

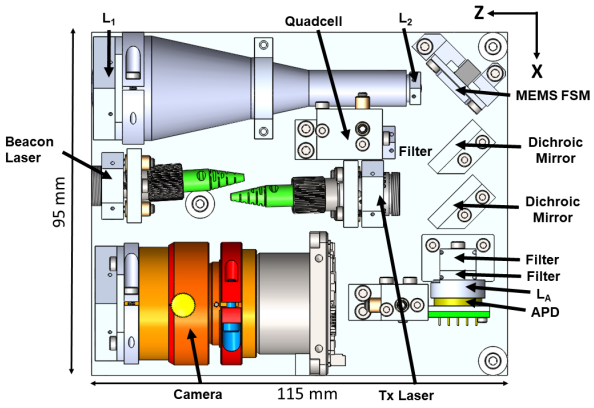

Figure 6: Assembly of Optical Components on Optical Bench

have a rim to hold the component, for support and alignment. Holes distributed radially around the optical component in each mount will allow for injection of room-temperature-vulcanizing (RTV) silicone during assembly. Stress is minimized on the optic by taking into account the coefficient of thermal expansion (CTE) of the optic, the cell (bezel), and the RTV, creating a low strain design.[16] The compliance of the RTV ensures that the CTE mismatch between the optic and the bezel does not distort the optic when thermal gradients occur.

Due to optical design constraints, it is necessary to determine if the stack up of machining tolerances of the optical mounts meets the tolerance requirements. Standard machining tolerances, even when reduced by a factor of 5, were identified as insufficient when implemented generically for all components through Zemax analysis in *Long*.[10] Therefore, some components are kinematically mounted to enable system calibration in the lab. A series of misalignment tolerance Monte Carlo analyses are used to determine the calibration adjustment ranges for resolution for rigid body tip, tilt, decenter, and piston for each element.[10] As the design is iterated, this probabilistic analysis is run to ensure that the payload manufacturing, assembly, and calibration process satisfies alignment requirements.

Kinematic mounting offers the necessary precision using adjustment screws (hex adjusters) while allowing typical manufacturing tolerances for the mounts. Implementation of a kinematic mount, such as the one shown in Fig. 2, requires trades between volume, alignment precision, and stability of the optics. Due to the volume constraints, the number of DOF of each kinematic mount are minimized to reduce the required mount volume. The fewer hex adjusters in the system, the fewer elements that must be secured

during assembly and the fewer elements subject to shift during launch. Table 1 identifies whether or not a kinematic mount is needed for each optical component. Kinematic mounts are reserved for the most sensitive optical displacement parameters. The kinematic mounting solutions selected for the quad-cell, APD, transmitting collimator, and beacon collimator include two DOF by assessment of the sensitivities. The sensor mounts adjust the decenter of the sensors while the collimator mounts adjust the tip/tilt of the laser. Adjustments in a kinematic mount are made using hex adjusters which each have a spherical tip on one end, the point of contact, and a hex socket, which can be turned to translate the spherical tip axially, on the other end. For DOF that do not require adjustment, stainless steel ball bearings will be bonded into counterbored holes to provide point contacts. The design for the kinematic mounts is adapted from the mechanical mount design in *Allan*.[8] As seen in Eq. (2) and Fig. 7, a kinematic mount with 16.75 mm between points of contact can be rotated 0.1° with an axial translation of 0.029 mm, which is satisfied by a 52.5° turn of the hex adjuster. Hence, a 45° turn of a M2.5 x 0.20 hex adjuster adequately adjusts the mount.

$$\theta = \arctan(\frac{x}{16.75 \text{ mm}}) = 0.1^\circ \quad (2)$$

$$x = 0.029 \text{ mm} \quad (3)$$

$$52.2^\circ \text{ turn of hex adjuster} \quad (4)$$

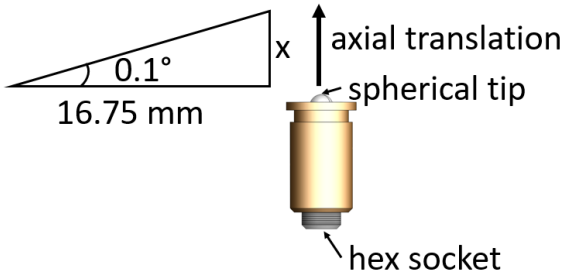

Figure 7: Axial translation for kinematic mount

The effect of the fine hex adjusters can also be recognized by the ratio of the fastener turning to the tip or tilt of the transmission collimator outside the payload. For the transmission collimator kinematic mount, it is found that for a 1.5° turn of the hex adjuster, the tip or tilt of the beam outside the telescope varies by 1 arcsecond. This is calculated using Eq. (5) and the angle definitions in Fig. 8:

$$\Delta x = l\Delta\theta_i \quad (5)$$

$$\Delta x = N_{\text{turns}} \cdot p \quad (6)$$

$$N_{\text{turns}} = \frac{\Delta\phi}{2\pi} \quad (7)$$

$$\Delta x = \frac{p\Delta\phi}{2\pi} \cong l\Delta\theta_i \quad (8)$$

$$\frac{\Delta\phi}{\Delta\theta_i} \cong \frac{2\pi \cdot l}{p} = 526.2\frac{\text{rad}}{\text{rad}} \quad (9)$$

$$\frac{\Delta\theta_o}{\Delta\theta_i} = \frac{1}{M_d} \cong \frac{1}{10} = 0.1 \quad (10)$$

$$\frac{\Delta\phi}{\Delta\theta_o} \cong 5262 = \frac{1.5^\circ}{\text{arcsec}} \quad (11)$$

where:

p = pitch of hex adjuster = $\frac{0.2 \text{ mm}}{\text{turn}}$

l = length between points of contact = 16.75 mm

M_d = angular magnification in telescope ≈ 10

$\Delta\theta_i$ = inside tip/tilt angle

$\Delta\theta_o$ = outside tip/tilt angle (outside telescope)

$\Delta\phi$ = adjustment angle of hex adjuster

Δx = translational adjustment

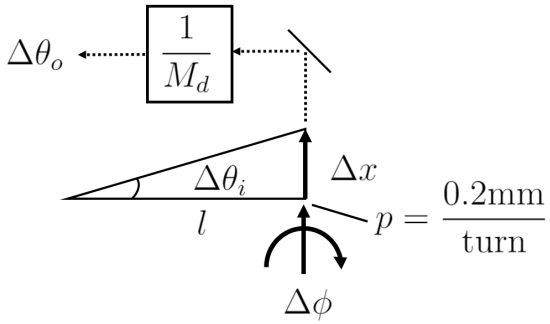

Figure 8: Definition of angles in calculation of ratio of fastener turn to tip/tilt of laser using kinematic mount.

In a similar manner, ratios of kinematic mount adjustment to component movement inside the payload can be characterized. The translational ratio of the kinematic mount is defined as the ratio of adjustment angle ($\Delta\phi$) to displacement along the axis of the adjuster (Δx). The rotational adjustment ratio is the ratio of the adjustment angle ($\Delta\phi$) to the tip/tilt angle inside the payload ($\Delta\theta_i$). When assembled, a kinematic mount has a translational ratio of $1.8^\circ/\mu m$ and a rotational adjustment ratio of 0.15°/arcsec without the telescope. Therefore, the

mount has a turning resolution of $\pm 27^\circ$ for $\pm 15 \mu m$ translation of the hex adjuster, as well as $\pm 4.5^\circ$ for ± 30 arcsec tip/tilt of the kinematic mount without the telescope.

During assembly of the payload, ground support equipment will be used to measure the locations of the optical components and dictate adjustments. The optical bench will be calibrated using the hex adjusters and custom ground support equipment, and preload will be applied to the mount. Then, the fasteners will be staked down with epoxy to ensure the calibrated positions of the optics are maintained.[17]

Optical Layout

After the components in need of kinematic mounts are identified, as listed in Table 1, the design requires trades between different versions of components, mounts of the components, and optical path layout. Of note are the sensitive and tight spacing requirements between the second telescope lens and Fast Steering Mirror (FSM) as well as between the FSM and the quadcell. These trades prompted the original design developed in *Long* to be iterated upon to produce the current design.[10] Fig. 9 illustrates the original design (a) from *Long* and the current design (b).

The original design from *Long* requires extremely tight spacing between the quadcell and APD sensors, with less than 1 mm between the outer diameters of the two sensors.[10] Implementing kinematic mounts for this spacing greatly increases the level of difficulty for assembly and calibration of the optical bench. The previous design also dictates atypical dimensions of the quadcell printed circuit board (PCB) with a width of less than 10 mm, as the quadcell board cannot interfere with the telescope barrel. Constraining the distance between the FSM and the first dichroic is the minimum bend radius of the fiber exiting the transmission collimator, 15 mm. This minimum bend radius must be observed to avoid signal attenuation and damage to the fiber.

Trading design requirements prompted several iterations before a balanced design was identified. The iterations occurred given the following considerations. The optical path length between the FSM and the quadcell must remain constant for a given design. However, the path lengths between the FSM and the first dichroic mirror and between the first dichroic mirror and the quadcell can be varied. Iterating the path lengths while maintaining a constant sum of the two parts resulted in the locations in the current design, Fig. 9(b).

Two options for the APD, shown in Fig. 10, are considered. The first, IAG200T6, offers a smaller package diameter and requires a larger PCB immediately attached to the board. The second option, RIP1-NJAF, presents a larger package diameter, requires a smaller PCB, and has higher performance. The diameter of the APD packaging is a significant matter, as the larger APD, RIP1-NJAF, with the higher performance presented problems for optical path lengths and fiber bend radii in the original design.

The successful optical layout and spacing design is shown in Fig. 9(b). Fig. 11 overlays the top view of the current CAD of the optical bench with the current optical spacing and path. It can be seen that spacing between the mounts for optical pieces, in particular between the quadcell and Tx Laser, are close together, but not interfering. The positions of the APD and the collimator, labeled as the Tx Laser in Fig. 9, are switched compared to the original design. This allows a longer, acceptable fiber radius leaving the collimator. In addition, it mitigates interference between the APD and quadcell optical pieces. This update also increases the APD's dependency on the alignment of the second dichroic, while decreasing the dependency of the Tx Laser on the second dichroic. The RIP1-NJAF APD, the larger of two APD options, is selected, as it requires a smaller PCB and offers higher performance. This became feasible due to the change in APD location.

The length and lens of the telescope are optimized through iteration using the Zemax software. The beam path through the telescope dictates the diameter of the telescope barrel. In turn, the diameter of the telescope barrel determines feasible positions of the quadcell, quadcell board, and mount. Minimizing the optical path diameter creates more space in the X direction for the quadcell. The completed assembly of optical components with kinematic mounts is shown in Fig. 6.

Thermoelastic Modeling Approach

The payload coarse pointing, acquisition, and tracking system uses a beacon-based approach to enable the spacecraft to detect, track, and point at each other. The beacon system consists of a 976 nm, 500 mW laser fixed in the payload (central aperture of Fig. 1) and a camera using an Aptina MT9P031 silicon complementary metal–oxide–semiconductor (CMOS) detector (right aperture of Fig. 1). The camera is used for closed-loop beacon feedback to the spacecraft following beacon acquisition. The beacon divergence angle must be sized to accommodate

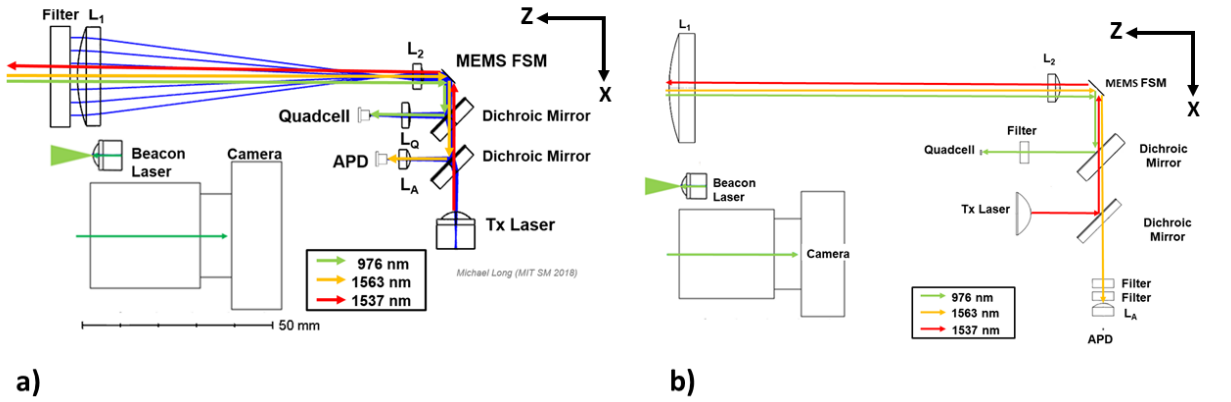

Figure 9: Comparison of Optical Path Designs a) Original Design by Long,[10] b) Current Design. Notable changes between the original design and the current design include the switching of the APD and Tx Laser locations, adjustment of spacing between the FSM, first dichroic, and quadcell, moving the filter location, and removal of the quadcell lens.

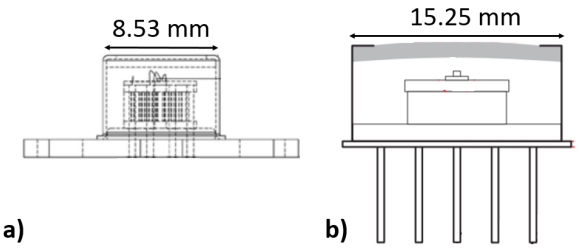

Figure 10: APD options under consideration during design iterations: a) IAG200T6 with a sensor housing diameter of 8.53 mm, b) RIP1-NJAF with a sensor housing diameter of 15.25 mm.

anticipated pointing errors with sufficient margin.[1] Due to the bistatic beacon optics design, thermoelastic shift must be budgeted as pointing error in the acquisition budget. The analysis is motivated by the need to quantify the dynamic uncertainty of the relative alignment between the payload apertures and the star trackers associated with thermoelastic deformation of structural components.

Kinematically, this is a relative attitude (tip/tilt) analysis, as longitudinal shifts are irrelevant in this case. There is only a single objective function which is the upper bound of misalignment. The analysis uses a simplified model of the spacecraft structure and thermal dynamics to estimate the objective. The thermal dynamics are modeled in Thermal Desktop® and used to load temperatures into a structural model in Femap®. These models are described in the following sections. The result of the

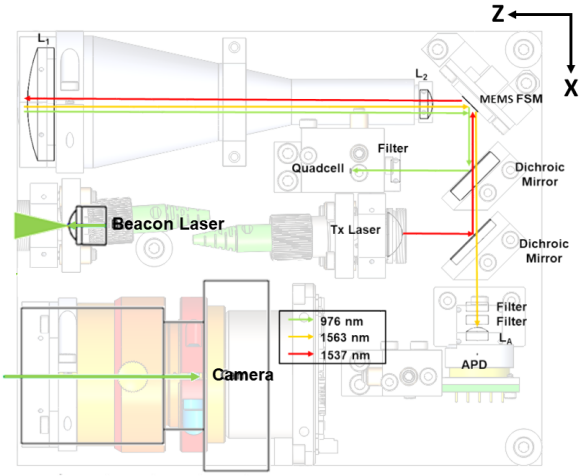

Figure 11: Top View of Current Optical Bench CAD Overlaid with Optical Path and Spacing

FEA is a time dependent mesh deformation. The upper bound on the relative misalignment between the payload apertures and the star trackers is calculated by statistical analysis of the attitudes of each element of the two possible payload faces (fore and aft) relative to the attitudes of each element of the possible star tracker faces. This value is used in the acquisition pointing budget to determine the acquisition margin calculated as a function of the roll-up of all acquisition uncertainties and the beacon divergence.

Thermal Model of the Bus

The Thermal Desktop® model for a 3U CubeSat for bus thermoelastic modeling is based on the Blue Canyon Technologies XB1.[18] The structure of the model is selected to be a hollow aluminum box with a thickness of 3.175 mm. The solar panels are modeled as thin pieces of FR-4 with thickness 2.5 mm. The optical properties of the hollow box are set to be aluminum tape with an emissivity of 0.04 and an absorptivity of 0.1. The optical properties of the sun-facing side of the solar panels are set to average solar cell optical properties with an emissivity of 0.85 and an absorptivity of 0.92. The backside of the solar panel has optical properties of black paint with an emissivity of 0.88 and an absorptivity of 0.88. The solar panels are thermally connected to the spacecraft structure with a conductance value of 0.5, an estimate of what the hinge conductance would be for the XB3. The main structure of the satellite has 351 nodes while the solar panels have 90 nodes. The model can be seen in Fig. 12.

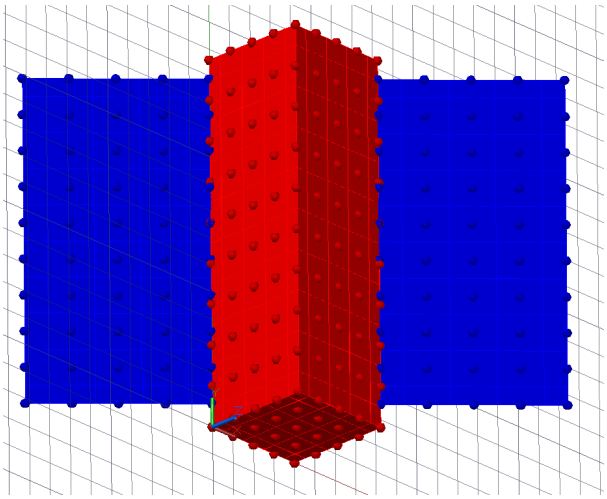

Figure 12: Thermal Desktop® model with 351 nodes on the main structure and 90 nodes on the solar panels.

The model is put into a LEO orbit modeled after that of the International Space Station with an inclination of 51.6° and an altitude of 400 km. The spacecraft is oriented so that the solar panels are always facing the sun. The thermal model is run for 185 minutes (> 2 orbits) with 1 minute time steps. At each time step, the nodes are exported with their location and temperature in Celsius.

Structural Model of the Bus

In conjunction with modeling the temperature of each spacecraft panel, a structural model of the spacecraft is developed. Femap® is selected as the tool for the structural model due to its finite element analysis, post-processing, and application programming interface (API) capabilities.

Detailed bus structural modeling information was not available at the time of this writing. Therefore, a generic 3U spacecraft of 0.100 m x 0.100 m x 0.340 m is created. The elements are defined as plates with 3.175 mm thick panels. Sensitivity analysis is performed to assess variability in the results with variations in structural parameters. The plates use the 6061-T651 Aluminum defined in the Femap® library. A mesh is created with a uniform spacing of 10 mm between nodes with 1562 nodes in total and is held constant across all timesteps.

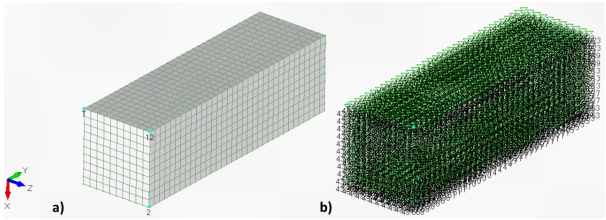

Figure 13: a) Femap® Model with mesh made up of 1562 nodes with edge length 1.0 cm making up 1560 elements. b) Femap® Model with Thermal Desktop® temperatures applied at each node.

A free-floating Finite Element Analysis (FEA) model can be constrained with the 3-2-1 method, in which one node constrains 3 DOF, a second node 2 DOF, and a third node the final DOF, as described by *Abbey*.[19] Fig. 13(a) shows the applied boundary conditions in the Femap® model with this methodology. Translation is constrained in all three directions at the -X, -Y, -Z corner, constrained in the X and Y directions at the -X, -Y, +Z corner, and constrained in the Y direction at the +X, -Y, +Z corner.

The quasi-static, isotropic structural model is propagated with the input from the thermal model. At each time step, the resulting thermal load is applied as a structural body load. The Thermal Desktop® nodal temperatures are mapped to the Femap® node locations using a MATLAB® script.

Each Femap® nodal temperature is defined as the temperature of the closest Thermal Desktop® node. A Femap® API loads the nodal temperatures, creates the appropriate load sets, applies nodal temperatures, initializes and runs analysis sets, then exports results for all nodes for a given number of timesteps. The temperatures applied at all nodes in one timestep are shown in Fig. 13.

Alternative formats to the structural model were also considered. Additional structural rigidity provided by a higher fidelity model has been found by a structural stiffness sensitivity analysis to be unnecessary. This is derived from the upper uncertainty bound being the objective, not the true mean misalignment. In particular, the effect of a 3.175 mm panel dividing the bus at Y = 15 mm is evaluated through the fraction of variance unexplained (FVU). The results of the higher fidelity model are calculated with Thermal Desktop® and Femap® models. In the calculation of the FVU, the "true" results are defined as the higher fidelity panel and the estimated values are defined as the lower fidelity results. These definitions calculate the FVU to be 0.14, implemented with the code in *Yenchesky*.[20] On a scale of 0 to 1, the better the prediction of the lower fidelity model, the lower the FVU. This indicates that the lower fidelity model is an appropriate prediction to use.

Results and Analysis

The results of the Femap® model at each timestep are loaded into the MATLAB® script for calculation and analysis of the thermoelastic pointing error. Two approaches are used: a location dependent calculation that uses the elements immediately surrounding the aperture and a calculation that considers the upper bound given all elements.

Location Dependent Approach

To calculate the pointing error, the location of the beacon on the +Y face of the bus is identified. Elements in the mesh of the model are identified such that the beacon location lies in central element with nodes A, B, C, and D, defined in Fig. 15. Combined with nodes E - L, the four nodes that border the central node are identified. Fig. 14 shows the beacon aperture frame of reference that should be used in all pointing error calculations. If a different frame of reference is used in the model, a change of basis should occur. The configuration can be seen in Fig. 16. The total, azimuth, and elevation thermoelastically induced bus pointing error with uncertainty at a given point is calculated using the following equations:

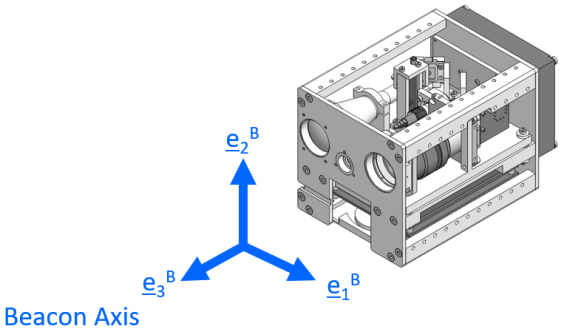

Figure 14: The frame of reference used in this calculation should be the beacon aperture frame $B = \{\underline{e}_1^B, \underline{e}_2^B, \underline{e}_3^B\}$.

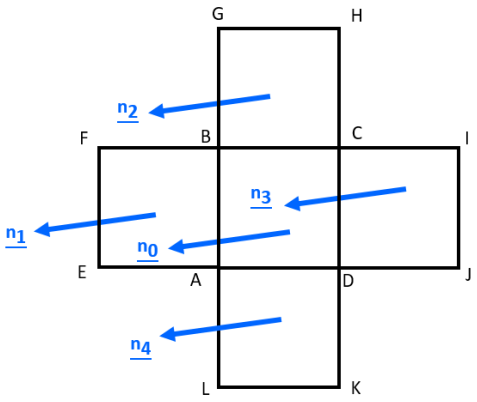

Figure 15: Beacon mesh around a central element 0 with neighboring elements 1 - 4.

Given $\underline{A}$ - $\underline{L}$ as the deformed points on the structural mesh, calculate the normal vectors, $\underline{n}_i$, for each element $i = 0$ to 4.

$$\underline{n}_0 = \frac{(\underline{B} - \underline{A}) \times (\underline{C} - \underline{A})}{\|(\underline{B} - \underline{A}) \times (\underline{C} - \underline{A})\|} \tag{12}$$

$$\underline{n}_1 = \frac{(\underline{F} - \underline{E}) \times (\underline{F} - \underline{B})}{\|(\underline{F} - \underline{E}) \times (\underline{F} - \underline{B})\|} \tag{13}$$

$$\underline{n}_2 = \frac{(\underline{G} - \underline{B}) \times (\underline{G} - \underline{H})}{\|(\underline{G} - \underline{B}) \times (\underline{G} - \underline{H})\|} \tag{14}$$

$$\underline{n}_3 = \frac{(\underline{C} - \underline{I}) \times (\underline{C} - \underline{D})}{\|(\underline{C} - \underline{I}) \times (\underline{C} - \underline{D})\|} \tag{15}$$

$$\underline{n}_4 = \frac{(\underline{A} - \underline{D}) \times (\underline{A} - \underline{L})}{\|(\underline{A} - \underline{D}) \times (\underline{A} - \underline{L})\|} \tag{16}$$

Calculate the average normal vector $\overline{n}$ using each of the five normal vectors:

$$\overline{n} = \frac{1}{4}\left(\underline{n}_0 + \underline{n}_1 + \underline{n}_2 + \underline{n}_3 + \underline{n}_4\right) \tag{17}$$

The confidence interval for small data sets and unknown population standard deviation is used:

$$u = t_{\alpha/2,r} \times \frac{S_{\overline{x}}}{\sqrt{n}} \tag{18}$$

$$r = n - 1 \tag{19}$$

$$n = 5 \tag{20}$$

$$\mu = \overline{x} \pm u \tag{21}$$

$$\tag{22}$$

At 99% confidence interval and n = 5, the uncertainty is generally written as:

$$u = t_{0.99,4}\frac{S_{\overline{x}}}{\sqrt{4}} = 2.0590 S_{\overline{x}} \tag{23}$$

$$\therefore u_{n_i} = K S_{n_i}, \text{for i} = 1, 2, 3 \tag{24}$$

Regarding the pointing error, quantities of note are the total, azimuth, and elevation pointing error. Total pointing error $\overline{\theta}_{tot}$ with uncertainty $u_{\theta_{tot}}$ is calculated as:

$$\overline{\theta}_{tot} = \arccos \overline{n}_3 \tag{25}$$

$$u_{\theta_{tot}} = \left|\frac{\partial \theta_{tot}}{\partial n_3}\right| = \frac{u_{n_3}}{\sqrt{1 - {n_3}^2}} \tag{26}$$

Azimuth pointing error $\overline{\alpha}$ with uncertainty u_α is calculated as:

$$\overline{\alpha} = \arctan \frac{\overline{n}_1}{\overline{n}_3} \tag{27}$$

$$\begin{aligned} u_\alpha &= \sqrt{\left(\frac{\partial \alpha}{\partial n_1} u_{n_1}\right)^2 + \left(\frac{\partial \alpha}{\partial n_3} u_{n_3}\right)^2} \\ &= \frac{\sqrt{\left(n_3 u_{n_1}\right)^2 + \left(n_1 u_{n_3}\right)^2}}{\left(n_1^2 + n_3^2\right)} \end{aligned} \tag{28}$$

Elevation pointing error $\overline{\epsilon}$ with uncertainty u_ϵ is calculated as:

$$\overline{\epsilon} = \arctan \frac{\overline{n}_2}{\overline{n}_3} \tag{29}$$

$$\begin{aligned} u_\alpha &= \sqrt{\left(\frac{\partial \epsilon}{\partial n_2} u_{n_2}\right)^2 + \left(\frac{\partial \epsilon}{\partial n_3} u_{n_3}\right)^2} \\ &= \frac{\sqrt{\left(n_3 u_{n_2}\right)^2 + \left(n_2 u_{n_3}\right)^2}}{\left(n_2^2 + n_3^2\right)} \end{aligned} \tag{30}$$

The translation in the X, Y, and Z directions of structural mesh nodes is used to calculate the azimuth, elevation, and total thermoelastically induced beacon pointing errors with respect to the spacecraft body frame. Figure 16 shows the thermoelastically induced pointing error over a single orbit, with the total thermoelastically induced pointing error ranging from 1.24 to 8.77 arcseconds.

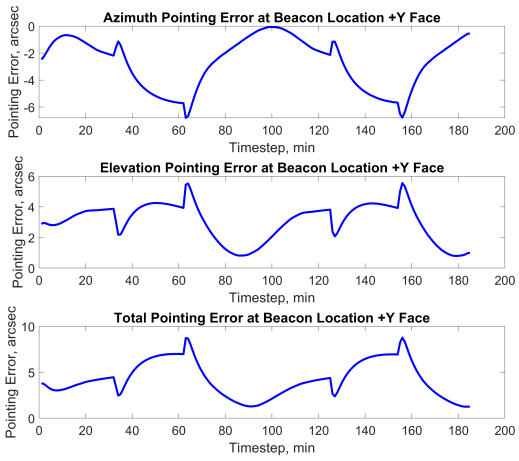

Figure 16: Azimuth, elevation, and total spacecraft pointing error induced by thermoelastic effects. The maximum uncertainties, calculated with 99% confidence, are 0.02, 0.02, and 0.02 arcseconds, respectively.

Relative Error Distribution Approach

While the location dependent approach provides an estimate for a specific aperture location, to estimate a maximum error bound, all face locations are considered. This also removes sampling bias from individual elements that are not representative of the structural bending modes of interest. Taking this broader approach, there are two faces designated as possible payload aperture sites (the fore and aft faces) and four faces designed as possible star tracker sites. Each cell on each face has a normal vector. In the reference undeformed state, the relative alignment between payload-type and star tracker-type faces is 90 degrees, which is zero misalignment. As the structure deforms, the normal vectors change and the motion of all of the normal vectors creates the statistical distribution.

To calculate this for a given timestep, the normal vector of every element on all six faces is calculated and classified as a payload-type or star-tracker type. All combinations of pairs of normal vectors (one from a payload face and one from a star tracker face)

are compared to calculate the relative angle. This angle is unbiased by subtracting 90 degrees and taking the absolute value. Taking the 99th percentile of all of the relative angles at each timestep provides a score that is stored for the timestep. The score for each timestep is calculated, producing another distribution, for which the 99th percentile is taken again, which gives the estimate of the upper bound of misalignment error. The result of this analysis over 185 timesteps can be seen in Fig. 17. The minimum 99% score at a single timestep is 2.56 arcseconds, while the maximum is 8.74 arcseconds.

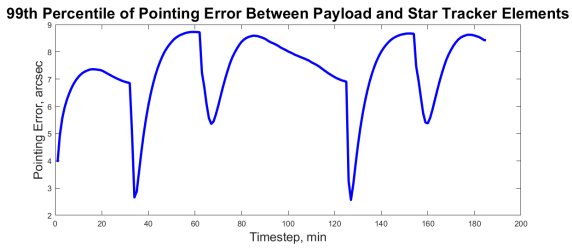

Figure 17: 99th percentile pointing error between payload and star tracker elements induced by thermoelastic effects. The maximum 99% score at a single timestep is 8.74 arcseconds.

Taking a histogram of the same data, seen in Fig. 18, the data is skewed to the right. The upper bound of misalignment error calculated as the 99th percentile of this data is 8.74 arcseconds. Fitting a distribution to the data, the extreme value distribution fit has a mean (μ) 7.87 and standard deviation (σ) 0.90 arcseconds.

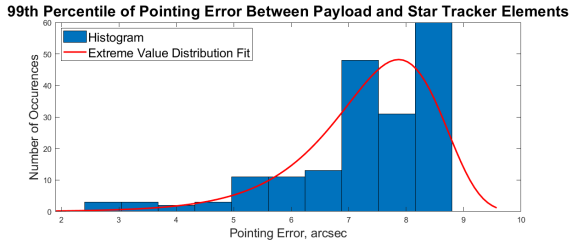

Figure 18: Statistical distribution of 99% total thermoelastically induced pointing error over 185 minutes. Extreme value distribution fit with mean (μ) 7.87 and standard deviation (σ) 0.90 arcseconds.

A number of sources of modelling error exist. The model uses the quasi-static assumption by breaking the full-continuum partial differential equations into static models of one minute time steps. Natural variation in the space environment has not been included in this study. There is also variability in structural rigidity depending on specifics of the bus design. There is also artificial variability due to mesh size selection.

A sensitivity analysis is conducted for structural rigidity and mesh size. To provide a baseline quantification of the variability due to structural rigidity, characterized by the wall-thickness, and due to mesh size. The variation in pointing error due to wall thickness can be locally linearly approximated via a computed elasticity of -0.096. Hence, to first order, an $\sim$ 1% increase in pointing error is induced for a 10% reduction in wall-thickness from the 3.175 mm value used. Therefore, the result is weakly variable for structural configurations similar to that used. The variability due to structural mesh size is highly nonlinear and not modeled at this time; however, representative simulation results are given for five different mesh sizes are given with element edge lengths ranging from 0.25 cm to 2.00 cm in Fig. 19. The maximum variation between any two mesh sizes is approximately 25%, and the worst case is used.

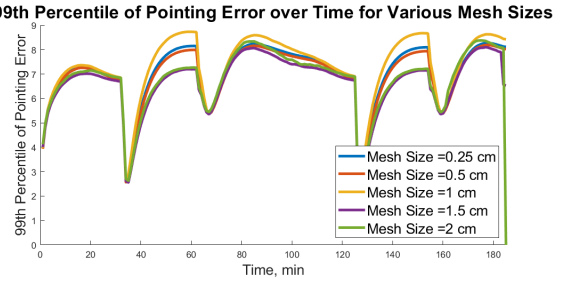

Figure 19: Sensitivity analysis of the effect of the mesh size on the 99th percentile of the pointing error.

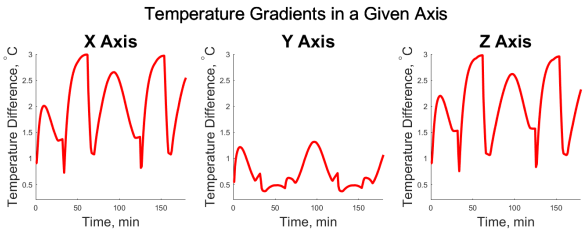

Figure 20: Thermal load in the X, Y, and Z directions.

Another metric of exploring the effect of the thermal gradient on the total pointing error induced by thermoelastic effects is the sample Pearson correlation coefficient.[21] The thermal gradient in the X, Y, and Z directions is calculated for a single time step as the absolute value of the maximum difference be-

tween the positive and negative faces in that direction. The thermal gradients are shown in Fig. 20. The sample Pearson correlation coefficient is calculated using: Eq. (31):

$$r_{xy} = \frac{\sum_{i=1}^{n}(x_i - \overline{x})(y_i - \overline{y})}{\sqrt{\sum_{i=1}^{n}(x_i - \overline{x})^2}\sqrt{\sum_{i=1}^{n}(y_i - \overline{y})^2}} \quad (31)$$

where the thermal gradient in a given direction is defined as x, the total pointing error as y, and the sample size as n. The sample Pearson correlation coefficients are determined to be 0.76, 0.30, and 0.72 for thermal gradients in the X, Y, and Z directions. The closer the coefficient is to 1, the more linear the relationship between the two parameters. It is shown here that the thermal gradient in the X and Z directions has a strong linear relationship with the total thermoelastically induced pointing error.

The total thermoelastic pointing error with respect to the spacecraft body frame is used in the acquisition pointing budget to determine the acquisition margin calculated as a function of the roll-up of all acquisition uncertainties and the beacon divergence. The pointing error allocation for thermally induced misalignment in a single axis is 295 arcseconds in *Long*.[10] The thermoelastically induced pointing error of 8.74 arcseconds is in two axes; so the corresponding single axis thermoelastically induced pointing error is less than 8.74 arcseconds. Therefore, the margin for the thermoelastically induced pointing error is greater than 32X.

Thermal Design and Model of the Payload

The thermal design of the payload is oriented around passive thermal control throughout most components. Passive thermal control was achieved through optimized conduction pathways designed to keep components within their operational temperatures as well as through the choice of components optical surface properties. The optical bench is designed with active thermal control to reduce thermal gradients across its structure. The reduction of thermal gradients as well as the temperature stability of the optical bench was kept in mind during design to limit the misalignment of optics. The optical bench is thermally isolated from the rest of the structure based on spacers designed to conduct heat poorly. A heater is also located on the bottom side of the optical bench to allow the temperature of the bench to be controlled within a specified range of temperatures.

A Thermal Desktop® model of the payload was built to model the transient thermal performance of the payload during storage and operation. The CAD model was replicated within Thermal Desktop and the appropriate material and optical surface properties were assigned to the finite difference bricks and surfaces that made up the model. The optical train was simplified to include the relevant components for transmit and receive. A rendering of the thermal model can be seen Fig. 21.

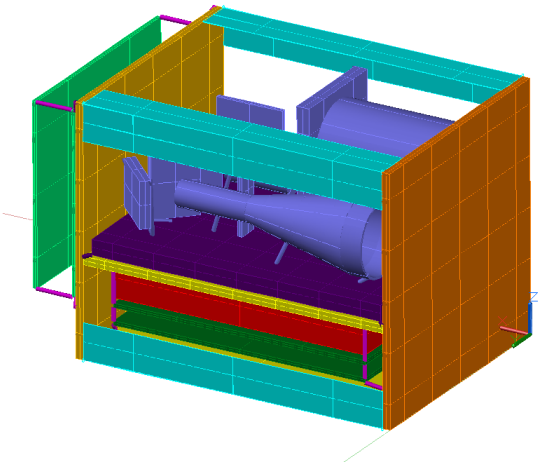

Figure 21: Thermal model of CLICK BC payload.

Two cases were run within Thermal Desktop. One model pertained to the standby mode of the payload. The standby mode has only the critical components turned on to have the payload communicate with the bus. The other model pertained to full-duplex transmit mode. The full-duplex transmit mode has all components outputting the full power they are drawing as heat. The difference between these models is the applied heat loads to the heat generating components in the payload simulating their operation. The current model simulates a 5 minute operational window before the operational temperature limits are met given conservative electronics power outputs. Electronics testing to refine power estimates is an ongoing effort. A second element of ongoing work is the development of a thermoelastic model for the optical bench based on the existing thermal model and a structure model of the optical bench. This model will utilize the same thermoelastic modeling process that was developed for the spacecraft bus.

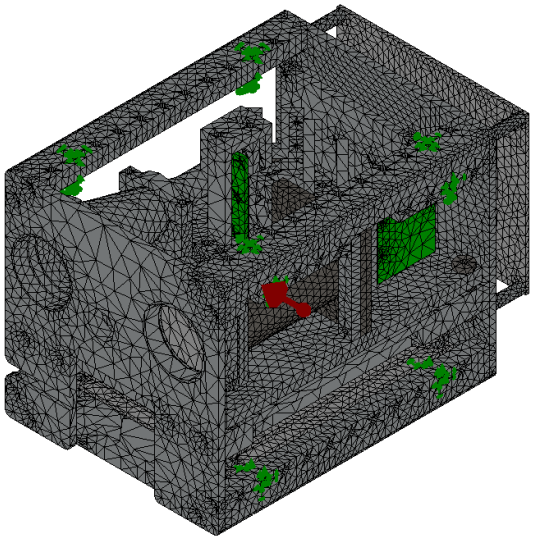

Figure 22: Finite Element Model for Structural Analysis. Fixed Geometry fixtures are present on both ends of both sides of all four rails at the second fastener hole from the end, or third if not available. The global component contact is defined as bonded.

Structural Analysis

FEA Model

Modal and static loading analyses are conducted on finite element models produced from the preliminary Solidworks® model, shown in Fig 4. The Solidworks® Simulation model used for both analyses uses a set of basic assumptions. Fixed constraints in the form of fixed geometry fixtures are located at the second from the end payload-bus interface holes, or the third hole if the second is not available. These constraints on the rails in the payload assumes that the bus is rigid. The connection between components is modeled as bonded, which treats the connected components as welded. This is a simplification compared to pinning connections between components and defining preload on the surface that bolt is providing a preload to. The way this is addressed is to have a bonded joints between components and then perform a separate fastener analysis. Fastener analysis, described in the following section, shows that all components are not expected to separate, shear, or exceed tensile loading abilities. The optical components as well as other negligible mass components, such as PCB-mounted components, are not included. Optical mounts containing RTV injection holes are simplified to remove the holes. The optical plate, Erbium Doped Fiber Amplifier (EDFA), and threaded spacers are also simplified to support meshing of the FEA model. The final mesh is shown in Fig. 22.

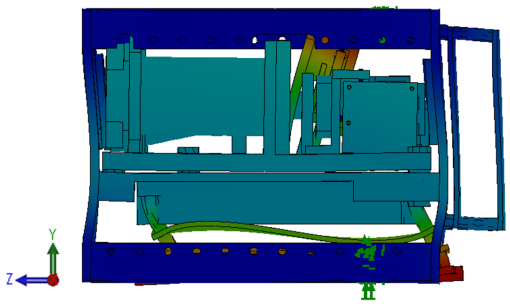

Figure 23: Results of modal analysis for CLICK payload. Lowest mode identified is 888 Hz and is located in the quadcell mount.

Modal Analysis

The modal analysis is conducted to determine the first resonant frequency of the CLICK payload. The resonant frequencies of the quadcell and APD boards are expected to be greater than 250 Hz at all modes. The first resonant frequency of the optical plate is calculated using Eq. (32) from Roark's Formulas for Stress and Strain which approximates the plate as a beam with both ends fixed and a center point load W.[22] The equation also assumes a uniform material with a modulus of elasticity of E, a moment of inertia of I, a gravity load of g, and length l.

$$f_1 = \frac{13.86}{2\pi} \times \sqrt{\frac{EIg}{Wl^3}} \tag{32}$$

The optical plate is made out of Aluminum 6061-T6 and assumed to carry a weight W equal to the mass of the optical bench, 0.47 kg, multiplied by the gravity, 9.81 m/s^2. The modulus of elasticity (E) of Aluminum 6061-T6 is 68.9 GPa. The base and height of the optical plate are 95 mm and 6 mm, respectively. The moment of inertia (I) is calculated using Eq. (33).

$$I = b \times \frac{h^3}{3} \tag{33}$$

Calculating the moment of inertia, I is found to be 1.71×10^{-9} m^4. Plugging this value into Eq. (32), the first resonant frequency of the optical plate is found to be 894 Hz. This is exceeds the minimum desired resonant frequency of 250 Hz with a factor of safety of 3.55.

Similar hand calculations for the rear board stack and bottom board stack are conducted. Eq. (33) finds the moment of inertia (I) to be $3.18 \times 10^{-11}\,\mathrm{m}^4$. Solving for the first resonant frequency with Eq. (32), the rear stack is predicted to have a first frequency of 567 Hz. Likewise, the bottom board stacks finds the moment of inertia to be $2.81 \times 10^{-11}\,\mathrm{m}^4$ and the first resonant frequency to be 278 Hz.

The resonant frequencies of the quadcell board are modeled with Table 16.1, Case 2b from Roark's Formulas for Stress and Strain[22] as a uniform beam with both ends fixed with Eq. (34):

$$f_1 = \frac{K_n}{2\pi} \times \sqrt{\frac{EIg}{Wl^3}} \tag{34}$$

where K_n is equal to 22.4 for the first mode. Using Eq. (33), the moment of inertia (I) is $3.03 \times 10^{-12}\,\mathrm{m}^4$. The first resonant frequency of the quadcell is estimated to be 3095 Hz. The equations, applied to the APD board, yield a moment of inertia (I) of $9.538 \times 10^{-12}\,\mathrm{m}^4$ and a first resonant frequency of 4904 Hz.

Modeling the quadcell mount structure as a uniform beam with left end fixed, the right end free (cantilever) and a load W on the right end from Table 16.1, Case 3a,[22] the first resonant frequency is estimated with Eq. (35):

$$f_1 = \frac{1.732}{2\pi} \times \sqrt{\frac{EIg}{Wl^3}} \tag{35}$$

The first resonant frequency of the quadcell mount is estimated to be 342 Hz. The geometry and masses used in all of the hand calculations are listed in the code in *Yenchesky*.[20]

Modal analysis is conducted with the finite element model to identify and locate the first resonant frequency of the payload. This analysis uses the model developed in Solidworks ® Simulation. The lowest mode identified is 888 Hz and is located in the quadcell mount, as shown in the analysis results in Fig. 23. The discrepancy between the hand calculation, 342 Hz, and the simulation results, 888 Hz, is attributed to the difference between the constraint definition in the hand calculation and finite element model. The quadcell mount connects to the bracket on two faces, increasing its rigidity; however, this is not reflected in the hand calculation. The five lowest resonant frequencies in the modal analysis and their locations are listed in Table 2. All of the resonant frequencies on the simulated payload are greater than 250 Hz with a factor of safety greater than 3.5.

Table 2: CLICK Payload Resonant Frequencies from Analysis

Mode No.	Freq. (Hz)	Components
1	888	Quadcell Mount
2	955	Quadcell Mount
3	1023	Bottom Board stack PCBs
4	1030	Bottom Board stack PCBs
5	1089	Fiber Raceway

Static Loading Analysis

Static loading analysis is performed to a load of 30 G, in accordance with NASA GEVS, on all three payload axes.[15] For each axis, the allowed stress ($\sigma_{\text{static yield}}$) is determined based on the material properties of each part and the static predicted stress ($\sigma_{\text{static predicted}}$) is calculated through FEA. As the material is strained and the material experiences stresses under the yield strength, the material elastically deforms. When the stress in the material exceeds the yield strength, the material plastically deforms. Fig. 24 shows this behavior for Aluminum 6061, where the sharpest bend in the curve occurs at its tensile yield strength. The MOS, calculated with Eq. (36), for each axis is expected to be greater than 0, the industry standard.[16] Most structural elements on the payload are made from Aluminum 6061 T6, which has a tensile yield strength of 276 MPa and a shear strength of 207 MPa.[23] The ball bearings, used for kinematic mounting, and standoffs are made from Type 304 Stainless Steel, which has a tensile yield strength of 215 MPa.[24] The thermal isolators, used for isolation of the EDFA and optical plates, are made from Titanium, which has tensile yield strength of 170 MPa and a shear strength of 240 MPa.[25]

The static predicted stress ($\sigma_{\text{static predicted}}$) is the maximum stress identified in the model. For ductile materials, including Aluminum 6061 T6, Type 304 Stainless Steel, and Titanium, the von Mises stress is used. The margin of safety is calculated using a desired factor of safety (FOS) of 1.25 with Eq. (36):

$$MOS = \frac{\sigma_{\text{static yield}}}{FOS \times \sigma_{\text{static predicted}}} - 1 \tag{36}$$

All MOSs for static loading in the CLICK payload calculated with Eq. (36) are greater than 0.

Static loading in the X, Y, and Z directions have MOS of 21, 44, and 16, respectively. The maximum stress locations for the X, Y, and Z locations are the 12 mm spacer in the bottom stack, the rail on the positive X - negative Y corner, and 3 mm standoff in the rear board stack, respectively. The current

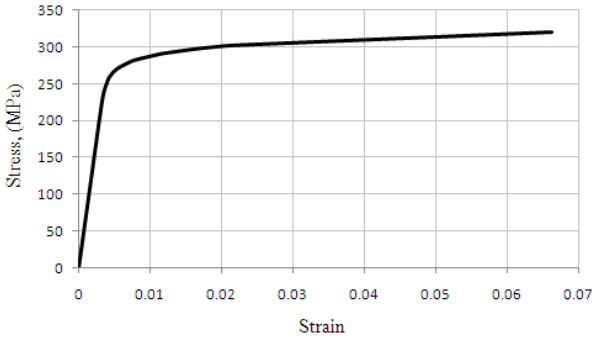

Figure 24: Stress-strain curve of Aluminum 6061-T6 under tensile loading. As the material is strained and the material experiences stresses under the yield strength (276 MPa), the Aluminum elastically deforms. When the stress in the material exceeds the yield strength, the material plastically deforms.

static loading model does not include the stiffness provided by fasteners or staking epoxies as a worst case. Hence, the fully assembled and staked hardware is expected to include higher MOS in the X and Z directions. The MOS is greater than 0, the desired MOS in all cases. Fig. 25 graphically depicts a typical loading with the Z axis case.

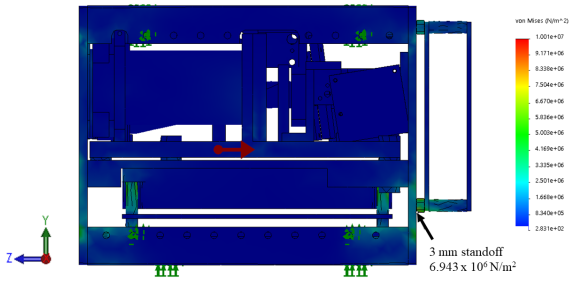

Figure 25: Static loading analysis results with loading in the Z axis. The highest von Mises stress and lowest MOS are located at the 3 mm standoff in the rear board stack.

FASTENER ANALYSIS

Separate from the static and dynamic loading models, hand calculations of fasteners are conducted to verify that mounted components will never separate, shear, or exceed the tensile loading abilities. The methodology is derived from the NASA Preloaded Joint Analysis Methodology for Space Flight Systems Memorandum,[26] as developed in Barnes.[16] Fastener analyses are conducted at a static loading of 30 G along each axis, in accordance with NASA GEVS, and calculating margins as done in Eq. (36).[15]

The analysis yields margins of safety in three cases: joint separation, pure shear loading, and pure tensile loading. The MOS is calculated as defined in Barnes and the desired value is 0 or greater.[16] The MOS for joint separation verifies that the external tensile load is not expected to exceed the internal compressive load. The MOS for pure shear loading confirms that the shear stress exerted on the fasteners is less than the stress at which the fasteners would begin to yield. The pure tensile loading compares the expected tensile loading to the tensile strength of the material.

Bus-Payload Interface

The bus-to-payload interface is assumed to be defined by 16 fasteners in total, with 4 fasteners on each of the +X, -X, +Y, and -Y sides. The fasteners are each M3 fasteners with 1 N-m of torque applied. The mass of the payload is assumed to be 1.5 kg under 30 G of loading. As a worst case assumption, only four of the fasteners are considered to be active.

The MOS for joint separation, pure shear loading, and pure tensile loading in the bus-payload interface case are 16, 27, and 14, respectively. Therefore, it is assumed that the fasteners will not separate or yield due to tensile or shear loads of 30 G.

EDFA to Optical Plate

The optical bench, which is the heaviest mounted subassembly, has an estimated mass of 471 grams, is secured to the EDFA plate using 3 M2.5 fasteners.

The MOS for joint separation, pure shear loading, and pure tensile loading in the bus-payload interface case are 19, 40, and 21, respectively. Since this bench is the heaviest mounted component and all fasteners are M2.5 or larger, it is assumed that all other mounted components will have higher MOS and subsequently will not separate or yield due to tensile or shear loads of 30 G.

Optical Components

The masses of each of the optical components and their mounts (portions not integrated into the optical bench) are considered. The camera and telescope are the two heaviest optical components and mounts.

Table 3: Margins of Safety on Optical Components with Mounts

Assembly	Joint Separation	Pure Shear Loading	Pure Tensile Loading
Camera	60	103	55
Telescope	251	467	245
Quadcell	511	868	466

The camera assembly has a mass of 178.79 grams and is mounted using 1 M2 and 2 M3 fasteners. The analysis set up does not accommodate multiple fastener sizes in one run, so the camera fastener input is simplified to 2 M3 fasteners. The telescope assembly has a mass of 17.94 grams and is mounted using two M2 fasteners. Additionally, the heaviest optical component and mount combination of the smaller optical components is identified as the quadcell assembly, with an estimated mass of 14.83 grams and mounted using two M2.5 fasteners. *Yenchesky* lists the reference data for these calculations.[20]

The margins of safety, calculated for joint separation, pure shear loading, and pure tensile loading are calculated for the camera, telescope, and quadcell assemblies. The results are summarized in Table 3.

As these are the heaviest optical element and mount pairs, it is expected that all other optical elements with their mounts have higher margins and will not separate or yield due to tensile or shear loads. Vibrations testing of engineering prototypes and the final payload units will be used to verify these analytical predictions.

CONCLUSIONS AND FUTURE WORK

The CLICK mission will play a role in enabling low-cost, low-complexity nanosatellites to communicate via laser crosslinks at high data rates. Pursuit of a successful design follows the many requirements dictated both by the program as well as self-imposed requirements, such as optical alignment tolerances.

The optomechanical design is a result of careful design decisions and trades, including the kinematic mounting technique. The current design satisfies the requirements of the mechanical, optical, and electronic subsystems. The kinematic mount technique is used for precision alignment. The bus thermoelastic analysis estimates, with uncertainty, that the total thermoelastically induced pointing error is 8.74 arcseconds; therefore, the margin of the thermoelastic pointing error allocation is greater than 32X. The current payload thermal model simulates a 5 minute operational window before the operational temperature limits are met given conservative electronics power outputs. Electronics testing to refine power estimates is part of ongoing work.

Results of structural and fastener analyses yield results above all recommended values. Multiple design iterations have produced the current design, which coordinates the many payload components and their requirements. Analysis of the preliminary design was conducted to verify requirements for the payload Preliminary Design Review (PDR) in April 2018. The design was refined to implement recent changes in payload components. The models used for simulations are updated and the analyses were repeated to ensure requirements continue to be met.

In addition to the thermoelastically induced bus pointing error, it is also important to understand thermoelastic deformations in the payload. The payload analysis studies the dynamic uncertainty of the relative alignment of optical elements within the payload. Kinemaically, this includes all DOF except roll (e.g. tip, tilt, piston, decenter). In particular there are three apertures that characterize three distinct optical trains that are mounted together on the same bench. These are the camera, beacon laser, and transmission and receiving chain. A payload analysis similar in approach to the bus analysis will be conducted at a later time for optical system requirements verification as well as a uncertainty bound in the fine pointing budget. This analysis will use thermal inputs from the bus provider when available. The software developed in this work lays the foundation for this future analysis.

Analyses will continue to be conducted for any future design refinements and as environmental inputs are refined. This will continue to support the precision pointing, acquisition, and tracking (PAT) system, made up of the CPS and fine pointing system (FPS). Anticipated bus pointing error induced by thermoelastic effects must maintain enough margin in the coarse pointing budget. Sound structural and fastener design must be maintained across the payload to support the optical instrument. Development of simulations, analyses, testing of non-flight models, and inspection upon assembly is anticipated to yield a successful design. Integration of all other subsystems will provide two nanosatellites that fulfill the CLICK mission. Future efforts after the CLICK mission may include refinement of the optomechanical design to accommodate changes necessary to expand the laser crosslinks to swarms and constellations.

ACKNOWLEDGEMENTS

The mission is a collaboration between the MIT Space, Telecommunications, Astronomy, and Radiation (STAR) Lab, University of Florida's Precision Space Systems Lab (PSSL), and NASA Ames Research Center (ARC).

REFERENCES

1. Peter Grenfell, Alexa Aguilar, Kerri Cahoy, and Michael Long. Pointing, Acquisition, and Tracking for Small Satellite Laser Communications, August 2018.

2. Matthew Smith, Amanda Donner, Mary Knapp, Christopher Pong, Colin Smith, Jason Luu, Peter Pasquale, and Brian Campuzano. On-Orbit Results and Lessons Learned from the ASTERIA Space Telescope Mission. *AIAA/USU Conference on Small Satellites*, August 2018.

3. Holly A. Bender, Pantazis Mouroulis, John M. Bellardo, Cole T. Gillespie, Grigory J. Heaton, Michael A. Fernandez, Nicholas N. Sizemore, Andres Andrade, Elliott H. Liggett, Peter Sullivan, Didier Keymeulen, Christopher D. Smith, and Megan Gibson. Snow and Water Imaging Spectrometer (SWIS): CubeSat configuration and design. In *CubeSats and NanoSats for Remote Sensing II*, volume 10769, page 107690B. International Society for Optics and Photonics, September 2018.

4. Demetrio Labate, Massimo Ceccherini, Andrea Cisbani, Vittorio De Cosmo, Claudio Galeazzi, Lorenzo Giunti, Mauro Melozzi, Stefano Pieraccini, and Moreno Stagi. The PRISMA payload optomechanical design, a high performance instrument for a new hyperspectral mission. *Acta Astronautica*, 65(9):1429 – 1436, 2009.

5. Schimmerohn et al. Additive Manufactured Structures for the 12u Nanosatellite ERNST. In *Additive Manufactured Structures for the 12U Nanosatellite ERNST*, pages 1–5. SSC18-WKVII-06.

6. Todd Rose, Darren Rowen, S. LaLumondiere, N. Werner, R. Linares, A. Faler, J. Wicker, C. Coffman, G. Maul, D. Chien, A. Utter, R. Welle, and S. Janson. Optical Communications Downlink from a 1.5u CubeSat: OCSD Program. *AIAA/USU Conference on Small Satellites*, August 2018.

7. Christian Fuchs, Christopher Schmidt, Jonas Keim, Florian Moll, Benjamin Rödiger, Michael Lengowski, Steffen Gaißer, and Dirk Giggenbach. Update on DLR's OSIRIS program and first results of OSIRISv1 on Flying Laptop. In *Free-Space Laser Communications XXXI*, volume 10910, page 109100S. International Society for Optics and Photonics, March 2019.

8. Gregory Allan, Ewan S. Douglas, Derek Barnes, Mark Egan, Gabor Furesz, Warren Grunwald, Jennifer Gubner, Christian Haughwout, Bobby G. Holden, Paula do Vale Pereira, Abigail J. Stein, and Kerri L. Cahoy. The deformable mirror demonstration mission (DeMi) CubeSat: optomechanical design validation and laboratory calibration. In *Space Telescopes and Instrumentation 2018: Optical, Infrared, and Millimeter Wave*, volume 10698, page 1069857. International Society for Optics and Photonics, August 2018.

9. Emily Clements, Raichelle Aniceto, Derek Barnes, David Caplan, James Clark, Inigo del Portillo, Christian Haughwout, Maxim Khatsenko, Ryan Kingsbury, Myron Lee, Rachel Morgan, Jonathan C. Twichell, Kathleen Reising, Hyosang Yoon, Caleb Ziegler, and Kerri Cahoy. Nanosatellite optical downlink experiment: design, simulation, and prototyping. September 2016.

10. Michael J. Long. Pointing Acquisition and Tracking Design and Analysis for CubeSat Laser Communication Crosslinks. Master's thesis, Massachusetts Institute of Technology, February 2018.

11. Katie M. Schwertz and Jim H. Burge. *Field Guide to Optomechanical Design and Analysis*, volume FG26. SPIE PRESS, August 2012.

12. Hamid Hemmati, editor. *Near-Earth Laser Communications*. CRC Press, Boca Raton, 2009.

13. Minotaur IV V VI User's Guide, August 2015. Release 2.2.

14. Roland Lagier. Ariane 5 User's Manual, 2016.

15. General Environmental Verification Standard, April 2013.

16. Derek Barnes. Optomechanical Design, Analysis, and Testing of the Nanosatellite Optical Downlink Experiment. Master's thesis, Massachusetts Institute of Technology, June 2018.

17. S. Salmon, M. Swank, G. D. Janaki Ram, B. E. Stucker, and J. A. Palmer. Effectiveness of epoxy staking of fasteners in aerospace applications. *Assembly Automation; Bedford*, 29(4):341–347, 2009.

18. RAVAN CubeSat Measures Earth's Outgoing Energy | NASA.

19. Tony Abbey. Free-Floating FEA Models, February 2015.

20. Laura Yenchesky. *Optomechanical Design for CubeSat Laser Infrared Crosslinks*. Undergraduate, Massachusetts Institute of Technology, May 2019.

21. Basic Concepts of Correlation | Real Statistics Using Excel.

22. Warren C. Young, Richard G. Budynas, and Raymond J. Roark. *Roark's Formulas for Stress and Strain*. 7th edition, 2002.

23. ASM Material Data Sheet, October 2018.

24. ASM Material Data Sheet, October 2018.

25. ASM Material Data Sheet.

26. Jeffery A. Chambers. NASA Preloaded Joint Analysis Methodology for Space Flight Systems Memorandum, December 1995.

ACRONYMS

APD avalanche photodiode. 5, 6, 8, 14, 15

API application programming interface. 9

CAD computer-aided design. 3–5

CLICK CubeSat Laser Infrared CrosslinK. 1, 2, 4, 5, 14, 15, 17

CMOS complementary metal–oxide–semiconductor. 7

CPS course pointing system. 3, 17

CTE coefficient of thermal expansion. 5

DeMi Deformable Mirror Demonstration Mission. 2

DOF degrees-of-freedom. 2, 3, 5, 6, 9, 17

EDFA Erbium Doped Fiber Amplifier. 14

ERNST Experimental Spacecraft based on Nanosatellite Technology. 2

FEA Finite Element Analysis. 9, 14, 15

FOS factor of safety. 15

FPS fine pointing system. 17

FSM Fast Steering Mirror. 7, 8

FVU fraction of variance unexplained. 10

FWHM full-width-half maximum. 2

GEVS General Environmental Verification Standard. 4

lasercom laser communications. 1

LEO Low Earth Orbit. 1, 9

MOS margin of safety. 4, 15, 16

NODE Nanosatellite Optical Downlink Experiment. 2

OCSD Optical Communications and Sensors Demonstration. 2

PAT pointing, acquisition, and tracking. 17

PCB printed circuit board. 7, 14, 15

PDR Preliminary Design Review. 17

PRISMA PRecursore IperSpettrale della Missione Applicativa. 2

RTV room-temperature-vulcanizing. 5, 14

SWaP Size, Weight, and Power. 2